



# Energy level mediation of $(\text{BiO})_2\text{CO}_3$ via Br doping for efficient molecular oxygen activation and ciprofloxacin photodegradation

Xin Hu<sup>a</sup>, Huiping Zhao<sup>a</sup>, Ying Liang<sup>b</sup>, Rong Chen<sup>a,\*</sup>

<sup>a</sup> School of Chemistry and Environmental Engineering, Wuhan Institute of Technology, Donghu New & High Technology Development Zone, Wuhan 430205, PR China

<sup>b</sup> School of Chemical Engineering, Hubei University of Arts and Science, Xiangyang 441053, PR China

## ARTICLE INFO

### Keywords:

$\text{Bi}_2\text{O}_2\text{CO}_3$

Molecular oxygen activation

Bromine doping

Energy level mediation

Ciprofloxacin degradation

## ABSTRACT

Solar-driven molecular oxygen activation is of great importance for reactive oxygen species (ROS) production in environmental remediation. In this work, a convenient bromine doping strategy was developed to mediate the energy level of  $\text{Bi}_2\text{O}_2\text{CO}_3$  for molecular oxygen activation. The band structure and DFT calculation demonstrate that the Fermi level of  $\text{Bi}_2\text{O}_2\text{CO}_3$  elevates after bromine doping, which promotes the molecular oxygen activation and ROS production. The Br-doped  $\text{Bi}_2\text{O}_2\text{CO}_3$  exhibits remarkably enhanced photocatalytic ability and could degrade 95% of the ciprofloxacin within 30 min. Moreover, HPLC-MS analysis elucidates that the pyrrolidone ring degradation process is the dominate pathway in ciprofloxacin degradation over Br-doped  $\text{Bi}_2\text{O}_2\text{CO}_3$ , resulting in the decrease of antimicrobial activity of the degradation products and the risk of drug-resistance. This work not only provides a molecular oxygen activation strategy via energy level mediation, but also helps us to further understand the relationship between the elemental doping and molecular oxygen activation.

## 1. Introduction

As one of the clean, strong and low-cost oxidant, molecular oxygen plays critical role in the chemical synthesis,  $\text{NO}_x$  removal and wastewater treatment [1–3]. Upon being activated, the generated reactive oxygen species (ROS), including superoxide radical ( $\text{O}_2^-$ ), hydroxyl radical ( $\text{OH}^\bullet$ ), singlet oxygen ( $^1\text{O}_2$ ), and hydrogen peroxide ( $\text{H}_2\text{O}_2$ ), possess different oxidation ability and function their own unique role in chemical reactions [4–6]. Unfortunately, most molecular oxygen activation cannot easily happen under mild condition because of spin forbidden reactions [7], which is highly related to the photogenerated electrons of catalysts. In the past decades, a series of photocatalysts have been developed for the molecular oxygen activation via various activation methods [8–11]. For examples, Zhang demonstrated that macroscopic polarization enhancement could promote charge separation, thus contributing to the molecular oxygen activation [12]. Dai found that cerium doping in bismuth molybdate could promote the process of single electron reaction between  $\text{Ce}^{3+}/\text{Ce}^{4+}$  and double electrons reaction between  $\text{Mo}^{4+}/\text{Mo}^{6+}$ , which is beneficial for the generation of superoxide radical ( $\text{O}_2^-$ ) and hydrogen peroxide ( $\text{H}_2\text{O}_2$ ), respectively [13]. However, there are still drawbacks and limitations in the reported strategies of the practical application of molecular oxygen activation. It is highly desirable to explore the strategy and understand the process of molecular oxygen activation.

Generally, n-type and p-type semiconductors could be evolved from intrinsic semiconductor by doping ions that could provide extra electron and holes, respectively [14]. Semiconductors with the electron-donating ions doping (n-type doping) would endow the materials “n-type” properties such as upshift of Fermi energy level and extra mobility of electron in conduction band. In contrast, introducing electron-withdrawing ions (p-type doping) would shift the Fermi energy of semiconductor down, which results in the valence band partially unoccupied [15,16]. As the activations of molecular oxygen on photocatalyst are strongly related to the electronic structure of semiconductor, the mediation of photocatalytic activity involving the molecular oxygen activation could be realized by ions doping [17,18].

Being a member of the Aurivillius family,  $\text{Bi}_2\text{O}_2\text{CO}_3$  consists of a  $(\text{Bi}_2\text{O}_2)^{2+}$  layers and  $\text{CO}_3^{2-}$  layers which could accelerate charge separation and transfer, and restrain the recombination of the photo-generated electrons and holes. Owing to those intrinsic properties,  $\text{Bi}_2\text{O}_2\text{CO}_3$  has attracted much attention owing to its widespread application in photocatalysis [19,20], sensing [21], antibacterial [22] and supercapacitor [23] in recent years. However,  $\text{Bi}_2\text{O}_2\text{CO}_3$  is a wide bandgap semiconductor with low light utilization and photocatalytic efficiency, which limits its application in photocatalysis. In order to improve the photocatalytic efficiency of  $\text{Bi}_2\text{O}_2\text{CO}_3$ , metal nanoparticles loading [24], construction of heterojunction [25], morphology control [26], and element doping [27] are applied to promote the

\* Corresponding author.

E-mail address: [rchenhku@hotmail.com](mailto:rchenhku@hotmail.com) (R. Chen).

<https://doi.org/10.1016/j.apcatb.2019.117966>

Received 25 May 2019; Received in revised form 6 July 2019; Accepted 15 July 2019

Available online 16 July 2019

0926-3373/ © 2019 Elsevier B.V. All rights reserved.

photocatalytic property of  $\text{Bi}_2\text{O}_2\text{CO}_3$ . Among these strategies, nonmetal element doping is widely reported. For examples, Dong et al. reported that carbon doping could broaden the light absorption range of  $\text{Bi}_2\text{O}_2\text{CO}_3$  and promote the removal efficiency of NO [28]. Zhao et al. found that antimony doping could increase the specific surface area and improve the efficiency of electrons transfer, thus contribute to the RhB degradation [29]. Qian verified that iodine doping could narrow the bandgap of BOC and enhance the absorption of visible light from theoretical calculation and experimental results [30].

Considering that  $\text{Bi}_2\text{O}_2\text{CO}_3$  is a n-type semiconductor with the majority carriers of electrons, the Fermi level is closed to the conduction band, which is beneficial in the process of molecular oxygen activation. It is because that the more positive conduction band (vs vacuum level) means the stronger ability of molecular oxygen activation in theory [31]. If we could mediate the conduction band, the controllable molecular oxygen activation and the production of reactive oxygen species could be realized. Motivated by the mediation of energy band structure of intrinsic semiconductor via doping, we intend to develop a convenient strategy to mediate the electronic structure of  $\text{Bi}_2\text{O}_2\text{CO}_3$  via bromine doping. It is considered that the conduction band of n-type semiconductor could be mediated by the introduction of electron-donating ions if the n type semiconductor is regarded as intrinsic semiconductor. Thus the ability of molecular oxygen activation of n-type semiconductor could be improved. Until now, it is seldom reported in photocatalytic systems. Therefore, if this assumption could be realized, it might be an interesting work.

In this work, Br-doped  $\text{Bi}_2\text{O}_2\text{CO}_3$  with different amount of bromine doping have been prepared through a facile hydrothermal method. With the introduction of bromine ion,  $\text{Bi}_2\text{O}_2\text{CO}_3$  shows more positive conduction band structure compared with vacuum level, which possesses stronger ability of molecular oxygen activation. The shift of Fermi level leads to the change of band structure. The more positive conduction band structure could promote the generation of reactive oxygen species, leading to highly efficient CIP degradation and two degradation pathway of CIP. To the best of our knowledges, there is almost no report on the energy level mediation for molecular oxygen activation via doping.

## 2. Experimental

### 2.1. Materials

Ciprofloxacin (CIP) and bismuth citrate (Bicit) were purchased from Aladdin (Shanghai, China). Sodium hydroxide (NaOH), sodium bromide (NaBr), potassium chloride (KCl), calcium chloride ( $\text{CaCl}_2$ ), magnesium chloride ( $\text{MgCl}_2$ ), ferric chloride ( $\text{FeCl}_3$ ), sodium bicarbonate ( $\text{NaHCO}_3$ ), sodium nitrate ( $\text{NaNO}_3$ ), sodium sulfate ( $\text{Na}_2\text{SO}_4$ ), sodium chloride (NaCl), ter-butyl alcohol (TBA), terephthalic acid (TA), and nitroblue tetrazolium (NBT) were purchased from Sinopharm Chemical Reagent (Shanghai, China). All the reagents were analytical grade without further purification.

### 2.2. Synthesis

$\text{Bi}_2\text{O}_2\text{CO}_3$  and Br-doped  $\text{Bi}_2\text{O}_2\text{CO}_3$  with different bromine doping amounts were prepared via a facile one-step hydrothermal process. In a typical synthesis, 1.592 g of bismuth citrate was added to 100 mL deionized water with constant stirring. Then the pH value of the solution was adjusted to around 8.5 by using 1 mol/L NaOH. Finally, the solution was transferred to a 150 mL Teflon-lined stainless steel autoclave and heated to 180 °C for 12 h. After the hydrothermal process, the suspension was centrifuged and washed with distilled water and ethanol for 3 times, and dried at 60 °C for 12 h (BOC). The Br-doped  $\text{Bi}_2\text{O}_2\text{CO}_3$  samples were prepared via the identical process, with the addition of 0.052 g (Br1-BOC), 0.103 g (Br2-BOC), 0.206 g (Br3-BOC), and 0.412 g (Br4-BOC) of NaBr into the 100 mL deionized water,

respectively.

### 2.3. Characterization

Powder X-ray diffraction (XRD) was carried out on Bruker axS D8 Discover ( $\text{Cu K}\alpha = 1.5406 \text{ \AA}$ ) in the range of 10° to 80°. Scanning electron microscopy (SEM) images were performed on Hitachi S4800 scanning electron microscope with an operating voltage of 5.0 KV. X-ray photoelectron spectra (XPS) were carried out on a VG Multilab 2000 photoelectron spectrometer ( $\text{Al K}\alpha$ ,  $2 \times 10^{-6} \text{ Pa}$ ). The Electron Spin Resonance (ESR) was performed on a Hitachi ESR spectrometer (JES, FA200). UV-vis diffuse reflectance spectra (DRS) were recorded on Hitachi spectrophotometer (UH4150). Fluorescence spectra (PL) were detected with a Hitachi fluorescence spectrophotometer (F4600). Total organic carbon (TOC) analysis of the solution was performed on an Elementar Vario TOC analyzer (Elementar, Germany).

### 2.4. Photocatalytic activity evaluation

Photocatalytic performance of the samples were evaluated by the photodegradation of CIP (10 mg/L) under UV-vis light irradiation by using a 240 W Xe lamp. In a typical photocatalytic experiment, 40 mg photocatalyst was dispersed into 80 mL CIP solution, and the suspension was stirred in dark for 1 h to ensure an adsorption-desorption equilibrium. Then the suspension was exposed to the light irradiation under 240 W Xe lamp. At each given time interval, 4 mL of the suspension was collected and centrifuged to remove the solid photocatalyst. The concentration of pollutant during the degradation was measured by Mapada spectrophotometer.

### 2.5. Analysis of the degradation pathway of ciprofloxacin

The degradation pathway of CIP was analyzed by high-performance liquid chromatography-mass spectrometry (HPLC-MS) technique (Agilent 1260/6310, Ion Trap LC-MS) equipped with an Agilent Model C18 column. The mobile phase composed of water (65%) and acetonitrile (35%, containing 0.2% formic acid) for CIP, and the flow rate was 0.2 mL/min. The gradient started with 20% acetonitrile or methanol, increased to 30% within 2.5 min and to 80% within 3.5 min, then returned to the initial composition within 5 min and equilibrated within 4 min. The injection volume was 20  $\mu\text{L}$ , and the column temperature was 30 °C. Mass spectrum was scanned in a  $m/z$  range from 100 to 450.

### 2.6. Determination of reactive oxygen species (ROS)

5,5-dimethyl-1-pyrroline-N-oxide (DMPO) was used as spin-trapping agent in the detection of the reactive oxygen species in ESR measurement, which was performed on a JES X-band ESR spectrometer under UV-vis light irradiation. 40  $\mu\text{L}$  of DMPO was added to the mixtures of sample and water or methanol to detect the superoxide radical and hydroxyl radical, respectively. The mixed suspensions were saturated in air with an injector and then irradiated for 5 min under UV-vis light irradiation.

The relative concentration of  $\cdot\text{OH}$  was also determined by a TA fluorescence method. 40 mg of the sample was added to 80 mL of the NaOH solution of TA ( $2 \times 10^{-3} \text{ mol/L}$ ), the solution was exposed to the light irradiation (China Education Au-light Co. Ltd, Beijing) for 30 min, then the fluorescence of the mixture test was measured on a Hitachi F-4600 fluorescence spectrophotometer with an excitation wavelength of 315 nm upon the light irradiation. NBT was used to determine the generation of  $\cdot\text{O}_2^-$  in the photocatalytic process. 40 mg sample was dispersed in 80 mL of the NBT aqueous solution ( $2.5 \times 10^{-5} \text{ mol/L}$ ), then the suspension was exposed under light irradiation (China Education Au-light Co. Ltd, Beijing). At each given time interval, 4 mL of suspension was sampled to determine the NBT concentration by

UV–vis spectrophotometer after centrifugation.

## 2.7. Photoelectrochemical experiment

The photoelectrochemical measurements were carried out on a CHI 660E electrochemistry workstation (Shanghai, China) consisted of standard three-electrode cell. The three-electrode cell for photocurrent measurement and Mott-Schottky experiment consists of platinum foil, saturated calomel electrode and working electrode. 0.5 mol/L  $\text{Na}_2\text{SO}_4$  solution was used as electrolyte solution. The working electrode was prepared according to the following process: 10 mg as-prepared sample was mixed with 0.5 mL DMF and 20  $\mu\text{L}$  nafion solution (5%, DuPont) to form homogeneous emulsion, then 40  $\mu\text{L}$  the catalyst emulsion was dropwise coated on a glass electrode. The three-electrode cell for electrochemical impedance spectroscopy (EIS) consisted of platinum foil, saturated calomel electrode and glassy carbon electrode, and 0.5 mol/L potassium ferricyanide solution was used as electrolyte solution.

## 2.8. Antibacterial activity test

*Escherichia coli* (CCTCC AB 90054) were selected as the model bacteria to evaluate the cytotoxicity of the photodegradation products of CIP. *E. coli* cells were first inoculated and cultured in 20 mL of Luria-Bertani liquid medium (2 g yeast extract, 4 g tryptone and 4 g NaCl dissolved in 400 mL deionized water) at 37 °C for 6 h in a shaking incubator. CIP and its photodegradation solution at 5, 10, 20 and 30 min were added to the LB liquid medium with equal volume, respectively. Then, 5% inoculation activated *E. coli* was added to the LB liquid medium with three replicates, respectively. The optical densities (OD) of the bacterial culture solutions at 600 nm after 12 h incubation were measured by using UV–vis spectrophotometry (UH4150).

## 2.9. Density functional theory (DFT) calculation

DFT calculations were performed in the Vienna ab initio simulation package (VASP). A spin-polarized GGA PBE functional, all-electron plane-wave basis set with an energy cutoff of 520 eV, and a projector augmented wave (PAW) method were adopted.  $\text{Bi}_2\text{O}_2\text{CO}_3$  is simulated using a surface model of p (1 × 1) unit cell periodicity. A Monkhorst-Pack mesh (3 × 3 × 1) was used for the Brillouin-zone integrations to be sampled. Electronic density of states (DOS) of supercells (1 × 1) was calculated using a higher 9 × 9 × 1 k-point mesh. The conjugate gradient algorithm was used in the optimization. The convergence threshold was set to 1 × 10<sup>−4</sup> eV in total energy and 0.05 eV/Å in force on each atom.

# 3. Results and discussion

## 3.1. Characterization

Fig. 1a shows the XRD patterns of the pristine BOC and Br-doped BOC samples, which demonstrates that all the patterns are well-indexed to orthorhombic  $\text{Bi}_2\text{O}_2\text{CO}_3$  (JCPDS

84-1752). With the increase of bromine doping, a slight peak shift of (013) and (110) plane could be found in the magnified XRD patterns, as depicted in Fig. 1b. It indicates that bromine ion might be incorporated into the lattices of BOC and results in the deformations of lattices. According to Bragg's law ( $d_{(hkl)} = a/\sqrt{h^2 + k^2 + l^2}$ ), the peak shift to a low angle reflects the lattice expansion caused by the substitution of the bromine with big radius for the oxygen with small radius [32], where  $d_{(hkl)}$ ,  $a$  and  $\theta$  is the distance between crystal planes of (h k l), the X-ray wavelength, and the diffraction angle of the crystal plane (h k l), respectively. Considering the binding energy of Bi–O and C–O, bromine prefers to substitute oxygen in [Bi–O] layer.

In order to confirm the bromine doping into lattice, X-ray

photoelectron spectroscopy (XPS) was used to detect the existence of bromine in the surface of samples. The full XPS spectra of BOC and Br3-BOC samples reveal the peaks of Bi, C, and O elements in BOC and Br3-BOC samples, as well as the Br element signal detected in Br3-BOC (Fig. S1, Supporting Information). In the high XPS spectra (Fig. 2), Bi 4f peaks centered at 159.2 and 164.6 eV are attributed to the vibration of Bi 4f<sub>7/2</sub> and Bi 4f<sub>5/2</sub>, respectively. O 1s peak could be divided into two peaks centered at 530.8 and 532.4 eV, which are ascribed to the vibration of Bi–O and C–O, respectively. C 1s peak centered at 288.6 and 284.7 eV are attributed to the vibration of O=C–O and adventitious carbon (AC), respectively. Obviously, the peaks attributed to the vibration of Bi 4f<sub>7/2</sub>, Bi 4f<sub>5/2</sub> and Bi–O all show a slight shift to the low binding energy in Br3-BOC, while no peak shift is found in the vibration of C–O and O=C–O and adventitious carbon. It further confirms that the lattice oxygen in [Bi–O] layers is more easily replaced by bromine than the lattice oxygen in [C–O] layer. SEM images demonstrate that the bromine doping has little influence on the morphology of BOC (Fig. S2, Supporting Information). The BET surface area of Br-doped BOC slightly increases from 20.0 (BOC) to 23.0 m<sup>2</sup>/g (Br3-BOC), which is probably ascribed to the element doping (Fig. S3, Supporting Information). Fig. 3 shows the EDX elemental mapping spectra of Br3-BOC, which further reveals the existence of Br in Br3-BOC and the uniform distribution of four elements (Bi, C, O and Br) in Br3-BOC.

## 3.2. DFT calculation

To clarify the effect of bromine doping on energy level mediation, density functional theory (DFT) calculation was first performed to predict the energy band structure of bromine doped  $\text{Bi}_2\text{O}_2\text{CO}_3$ . The molecular structure models (Fig. 4a and b) are built by replacing lattice oxygen in [Bi–O] layer with bromine according to the previous results of XRD and XPS analysis. The PDOS of pure BOC and Br-doped BOC are depicted in Fig. 4c and d, which shows that the orbitals of Bi and O atoms are mainly responsible for developing conduction band edge and valence band edge. Compared the PDOS and calculated band structures of BOC with Br3-BOC (Fig. 4e and f), positive shifts are found in both the conduction band edge and valence band edge of Br3-BOC (vs vacuum). Moreover, a doping level is generated in Br3-BOC, which is close to the conduction band edge, leading to the positive shift (vs vacuum) of conduction band. The more positive conduction band is, the stronger ability of molecular oxygen activation the sample presents.

## 3.3. Energy level structure

The ultraviolet-visible diffuse reflectance spectroscopy (DRS) is performed to determine the light absorption range and band structure of BOC and Br-doped BOC samples. As shown in Fig. 5a, the absorption edge of pristine BOC is around 350 nm. With the Br doping, the absorption spectra of the Br-doped BOC samples show a red shift, indicative of a wider light absorption range after bromine doping. Accordingly, the bandgap shrinking is also found in the bandgap energies, as illustrated in the inset of Fig. 5a. The result illustrates that the doping of bromine could narrow the bandgap of BOC, which is consistent with DFT calculation. Furthermore, the Mott-Schottky and VB-XPS were employed to determine the VB and CB position as well as the bandgap of the semiconductor. As shown in Fig. 5b, the flat band potential of BOC, Br1-BOC, Br2-BOC, Br3-BOC and Br4-BOC is -0.31, -0.51, -0.58, -0.62 and -0.66 V, respectively, versus the saturated calomel electrode (SCE), which corresponds to 0.35, 0.15, 0.08, 0.04 and 0 V versus the normal hydrogen electrode (vs NHE). According to the reported literature, the flat band potentials of n type semiconductor is close to the Fermi level [31], therefore, the Fermi level of BOC and Br3-BOC is 0.35 and 0.04 V, respectively. VB-XPS spectra (Fig. 5c) reveals the energy gap between Fermi level and valence band, and the VB position of BOC and Br3-BOC is calculated to be 3.10 and 2.59 V, respectively. Based on the formula ( $E_{\text{CB}} = E_{\text{g}} - E_{\text{VB}}$ ), the CB position of BOC and Br3-BOC is

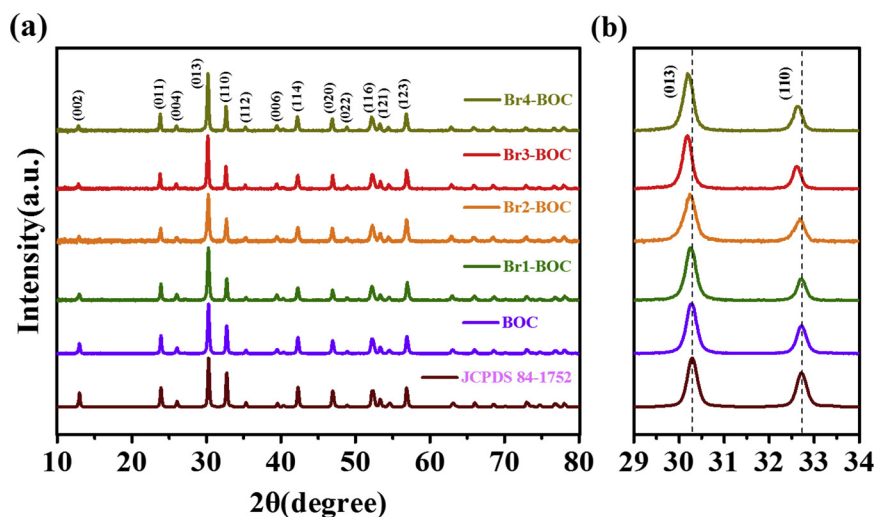


Fig. 1. XRD patterns (a) and the magnified XRD pattern (b) of  $\text{Bi}_2\text{O}_2\text{CO}_3$  and Br-doped  $\text{Bi}_2\text{O}_2\text{CO}_3$  samples.

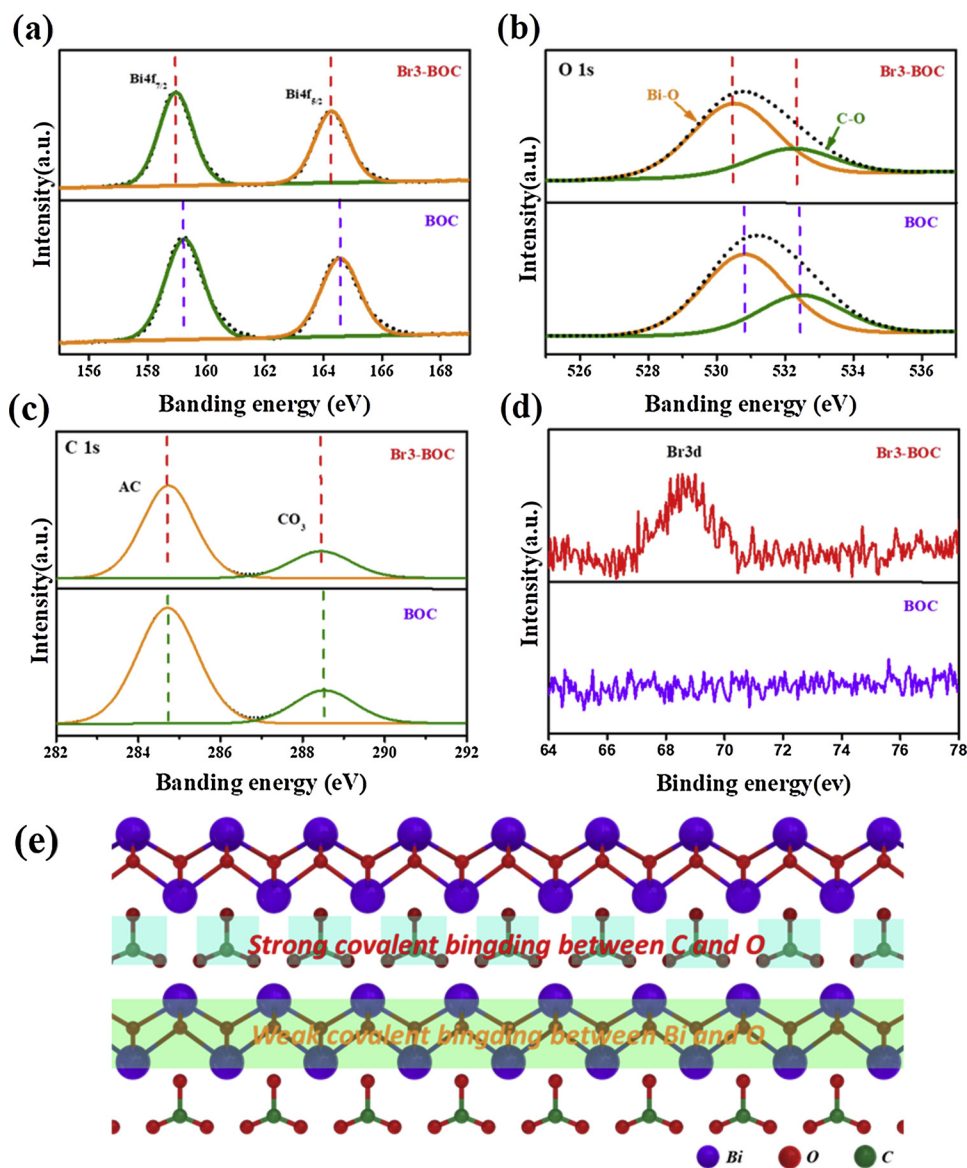


Fig. 2. High-resolution XPS spectra of BOC and Br3-BOC. Bi 4f (a), O 1s (b), C 1s (c), and Br 3d (d). Schematic illustration of the layer structure of the bromine substitution of lattice oxygen in Bi–O layer instead of C–O layer in  $\text{Bi}_2\text{O}_2\text{CO}_3$  crystal (e).

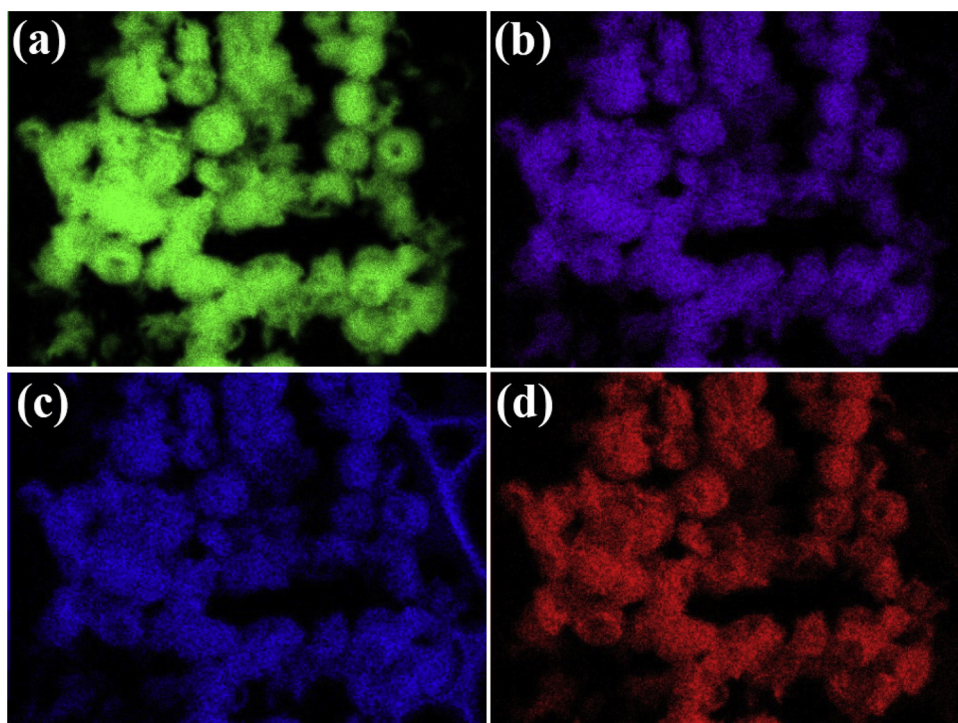


Fig. 3. EDX elemental mapping of Br3-BOC. Bi (a), Br (b), C (c) and O (d).

determined to be  $-0.10$  and  $-0.44$  V (Table S2, Supporting Information), respectively. As is illustrated in Fig. 5d, the conduction band position of BOC ( $-0.10$  V) is positive than the potential of molecular oxygen activation ( $O_2/\cdot O_2^-$ ,  $-0.33$  V vs NHE), which suggests that BOC sample could not activate molecular oxygen to generate superoxide radical. However, Br3-BOC exhibits more negative conduction band position ( $-0.44$  V vs NHE) due to energy level mediation after Br doping, which could provide enough potential for the molecular oxygen activation to generate superoxide radical. Based on the above results, it is believed that the energy level mediation of Br3-BOC is beneficial for the molecular oxygen activation.

### 3.4. Determination of reactive oxygen species

In order to verify the molecular oxygen activation after bromine doping, electron spin resonance (ESR) spectra was carried out to detect the generation of reactive oxygen species. Fig. 6a and b shows the ESR spectra of DMPO- $\cdot O_2^-$  and DMPO- $\cdot OH$  signals of BOC and Br3-BOC samples. As expected, Br3-BOC displays an obvious characteristic peak of  $\cdot O_2^-$  and  $\cdot OH$  upon light irradiation, while BOC only shows a weak ESR signal of  $\cdot OH$  and almost no ESR signal of  $\cdot O_2^-$  is detected in BOC sample. It illustrates that the molecular oxygen activation ability of Br3-BOC is much higher than that of BOC, leading to the production of more  $\cdot O_2^-$  and  $\cdot OH$  over Br3-BOC sample. To further confirm the origin of

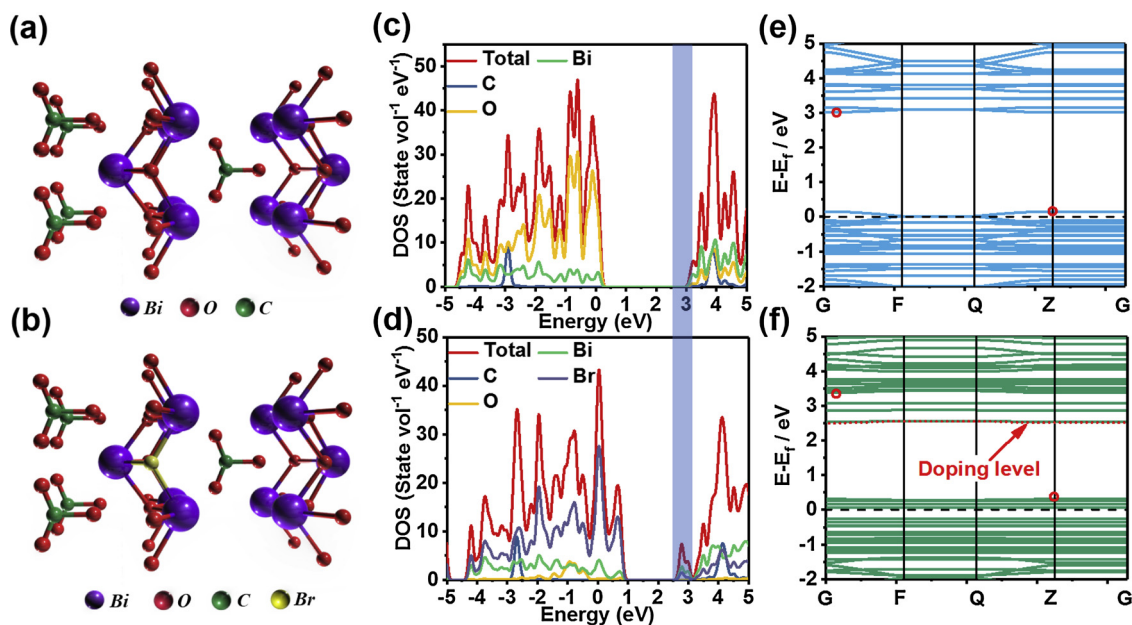


Fig. 4. Crystal structure of BOC (a) and Br3-BOC (b). Total density of states of BOC (c) and Br3-BOC (d) and calculated band structures of BOC (e) and Br3-BOC (f).

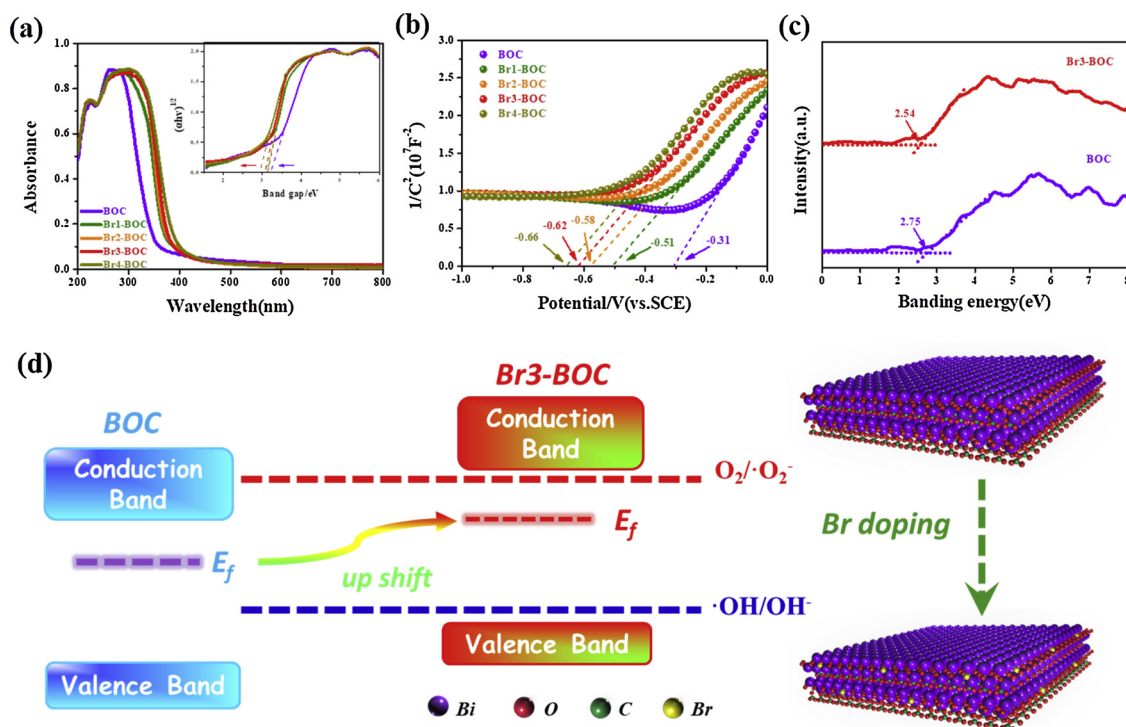


Fig. 5. UV-vis absorption spectra and the bandgap energies (a), Mott-Schottky plots (b) and VB XPS spectra (c) of the prepared BOC and Br3-BOC samples. Schematic illustration of the energy level tuning process and corresponding energy level (d).

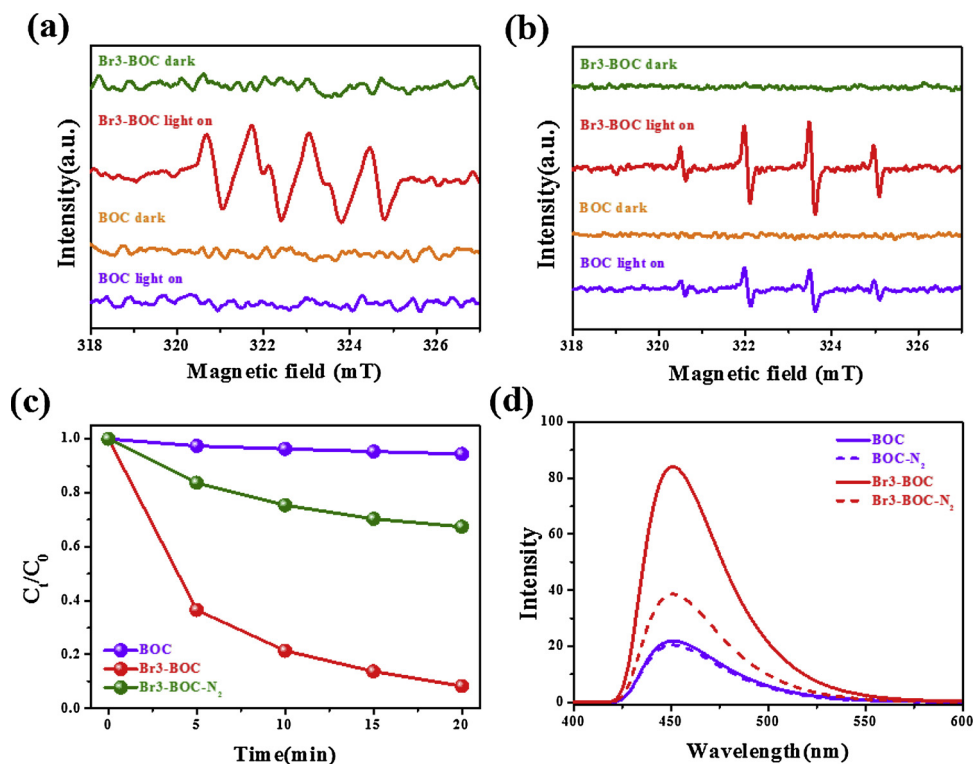


Fig. 6. The DMPO- $\cdot O_2^-$  (a) and DMPO- $\cdot OH$  (b) EPR spin-trapping spectra of BOC and Br3-BOC samples upon light irradiation. NBT photocatalytic oxidation (c) and TA-NaOH fluorescence spectra (d) over BOC and Br3-BOC samples.

reactive oxygen species, trapping agent experiment are also carried out. As shown in Fig. 6c, Br3-BOC possesses the higher photocatalytic ability and faster reaction rate for nitroblue tetrazolium (NBT) transformation, indicating that Br3-BOC is favorable to the generation of abundant  $\cdot O_2^-$ . Besides, it is also found that the photocatalytic NBT oxidation

was significantly inhibited in the present of  $N_2$ , further verifying the molecular oxygen activation process in the generation of  $\cdot O_2^-$ . Fig. 6d shows the TA-NaOH fluorescence spectra of BOC and Br3-BOC upon light irradiation, it demonstrates that the relative concentration of  $\cdot OH$  produced by Br3-BOC estimated by TA-NaOH fluorescence method is

higher than that of BOC, which is consistent with the ESR results. The obviously decreased signal of  $\cdot\text{OH}$  is observed over Br3-BOC sample in the presence of  $\text{N}_2$ , while no change of  $\cdot\text{OH}$  signal is detected in BOC sample, also indicative of the molecular oxygen activation process. Noticeably, a certain amount of  $\cdot\text{OH}$  still could be generated in the presence of  $\text{N}_2$ , illustrating another process of  $\cdot\text{OH}$  generation except for the molecular oxygen activation process. It is proposed that the production of  $\cdot\text{OH}$  over Br3-BOC in the presence of  $\text{N}_2$  and the generation of  $\cdot\text{OH}$  over BOC are mainly attributed to the oxidation of water molecular by the photogenerated holes. The previous data demonstrates that the valence band of Br3-BOC is more negative than that of BOC (vs NHE), indicative of weaker ability of water oxidation. However, it is found that the peak intensity of  $\cdot\text{OH}$  generated by Br3-BOC in the present of  $\text{N}_2$  is still stronger than that of BOC, suggesting that Br3-BOC could produce more  $\cdot\text{OH}$  than BOC whether in the presence or in the absence of  $\text{O}_2$ . The generation of  $\cdot\text{OH}$  is related to the water oxidation ability of holes in the absence of oxygen and the amount of holes. Therefore, it is believed that more photogenerated holes are produced over Br3-BOC, resulting in generating more  $\cdot\text{OH}$ , although Br3-BOC has weaker ability of water oxidation. To verify this speculation, the interfacial charge transfer on the surface of BOC and Br-doped BOC are investigated. Fig. 7a and b show the surface charge density and photoluminescence (PL) spectra of BOC and Br-doped BOC. Compared with pure BOC sample, Br-doped BOC samples display higher photocurrent density and lower fluorescence intensity, indicative of higher separation efficiency and lower recombination efficiency of electrons and holes through the energy level tuning strategy. Br3-BOC possesses the highest photocurrent density and lowest fluorescence intensity, which illustrates that the enhanced separation efficiency and lower recombination efficiency lead to the generation of more holes, thus resulting in more  $\cdot\text{OH}$  production, even in the present of  $\text{N}_2$ . Besides, the electrochemical impedance spectroscopy (EIS) Nyquist plots also illustrated that the Br3-BOC sample showed the faster interfacial charge transfer characteristics than that of BOC (Fig. S4, Supporting

Information). The illustration of the charge separation and recombination of BOC and Br-doped BOC is schematically depicted in Fig. 7c.

### 3.5. Photocatalytic activities

It is reported that the photodegradation of CIP is closely related to the reactive oxygen species [33]. Hence, CIP is selected as the target pollutant to evaluate the photocatalytic activity of Br-doped BOC samples. As shown in Fig. 8a, BOC could only degrade 35% of the CIP within 30 min. With the increase of Br doping amount, the degradation efficiency gradually enhanced, and Br3-BOC exhibits highest efficiency of degradation, which could degrade 95% of the CIP within 30 min. Compared with the reported photocatalysts for CIP degradation, Br-doped BOC exhibits remarkably superior photocatalytic performance for the degradation of CIP, as summarized in Table S1 (Supporting Information). However, the photodegradation efficiency of Br-doped BOC decreased after excessive bromine doping, and Br4-BOC could only degrade 82% of the CIP within 30 min. It might be attributed to the formation of recombination centers of photogenerated electrons and holes after excessive amount of Br doping, which is confirmed by the stronger fluorescence peak of Br4-BOC than that of Br3-BOC, indicating a faster recombination rate of electrons and holes, as shown in previous fluorescence spectra (Fig. 7b). The kinetics of CIP degradation over BOC and Br-doped BOC samples also reveal the CIP degradation fits well as pseudo-first-order. Br3-BOC shows fastest photocatalytic reaction rate with an apparent rate constant of  $0.086 \text{ min}^{-1}$ , which is approximately 7.7 times high than that of BOC (Fig. 8b). It indicates that the bromine doping is an effective strategy to promote the photocatalytic efficiency of BOC.

In order to confirm the effect of ROS in the degradation of CIP, the trapping experiments are performed by using  $\text{N}_2$ , IPA and OA as the scavenger of  $\cdot\text{O}_2^-$ ,  $\cdot\text{OH}$  and hole, respectively. As depicted in Fig. 8c, all of  $\cdot\text{O}_2^-$ ,  $\cdot\text{OH}$  and  $h^+$  contribute to the degradation of CIP over Br3-

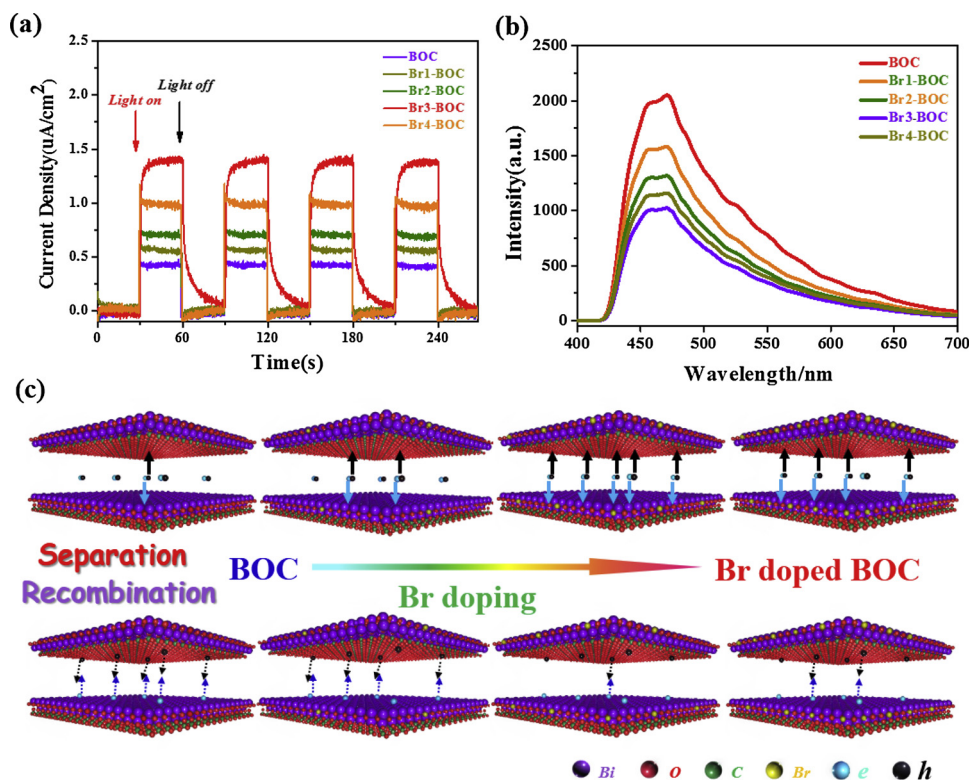
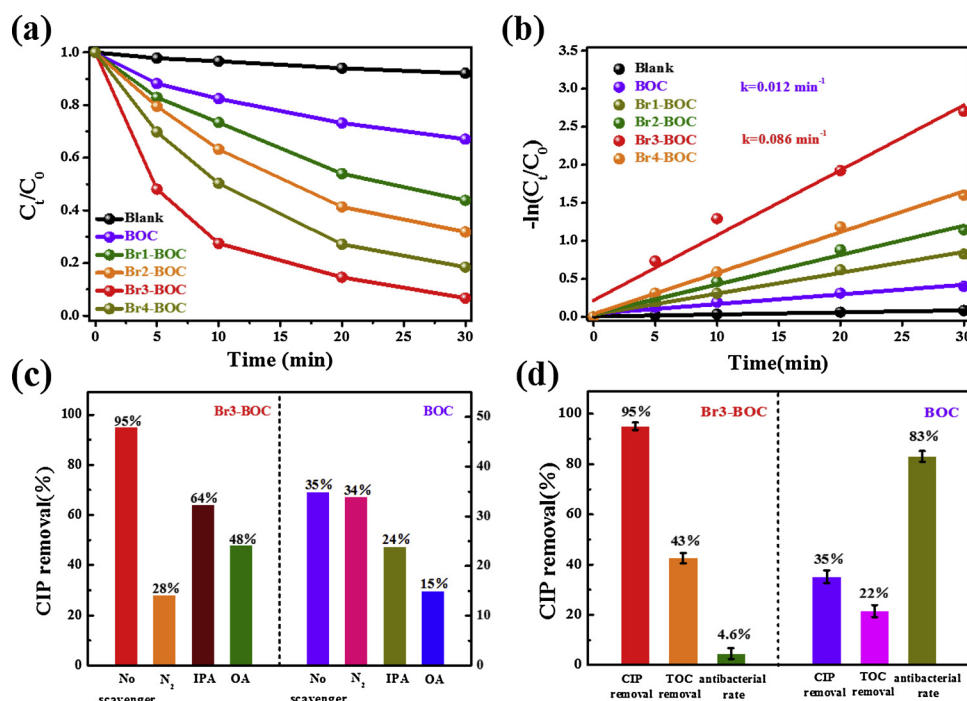


Fig. 7. Photocurrent density (a) and photoluminescence spectra (b) of BOC and Br-doped BOC samples; Schematic illustration of the separation and recombination of electrons and holes in BOC and Br-doped BOC (c).



**Fig. 8.** Photodegradation efficiency (a) and kinetic curves (b) of CIP degradation over BOC and Br-doped BOC; Photodegradation efficiency of CIP in the presence of different scavengers (c), CIP degradation efficiencies, TOC removal efficiencies and antibacterial activities of the degraded CIP solution over BOC and Br3-BOC (d).

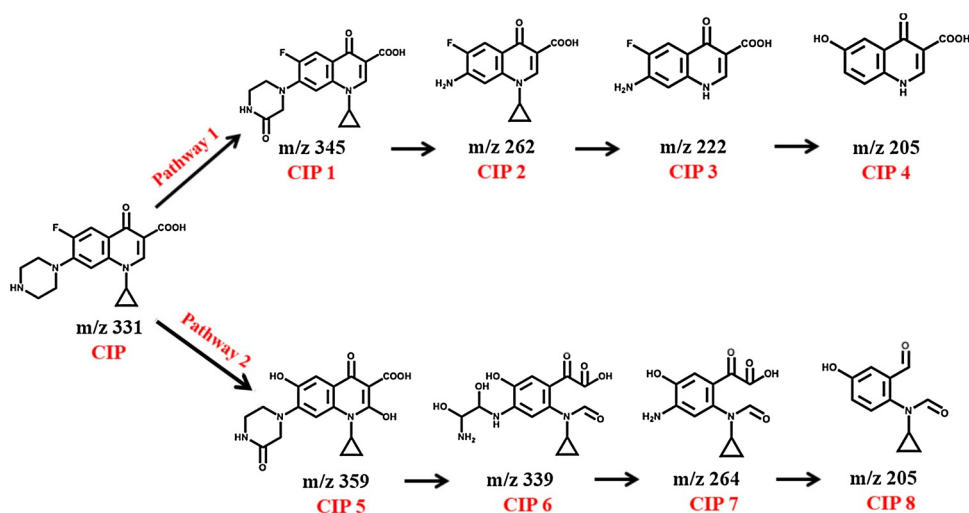
BOC, and  $\cdot O_2^-$  is the dominant reactive oxygen species in the degradation of CIP. The degradation efficiency of CIP decreases from 95% to 28% under  $N_2$  atmosphere, illustrating that Br3-BOC generates  $\cdot O_2^-$  via a molecular oxygen activation process. Nevertheless, almost no change is observed in CIP degradation efficiency of BOC in the presence of  $N_2$  atmosphere, demonstrating that the molecular oxygen activation process is not involved in the CIP degradation over BOC.  $\cdot OH$  and hole are the main active species in the CIP degradation over BOC, which could be significantly inhibited in the presence of IPA and OA (Fig. 8c, right). Combined with the ESR results, it could be concluded that BOC realizes the activation of molecular oxygen via bromine doping.

More importantly, it is found that Br3-BOC also exhibits higher TOC removal efficiency, which is nearly two times higher than that of BOC (Fig. 8d). The different mineralization in CIP degradation indicates the different intermediate products in BOC and Br3-BOC system. Therefore, the antibacterial ability of intermediate products during CIP degradation over BOC and Br3-BOC are evaluated by using *E. coli* as the model bacteria. It is found that the inhibition rate of CIP degradation products over Br3-BOC decreased rapidly after 30 min photocatalytic reaction, indicating that the degradation products completely lost their antibacterial abilities towards *E. coli*. However, the CIP degradation products over BOC remain the high the antibacterial activity (83%) towards *E. coli* (Fig. 8d). It indicates that the bromine doping strategy not only endows Br3-BOC high CIP degradation and mineralization efficiency, but also makes the degradation products lost the antibacterial ability, which could avoid drug resistance and the second pollution effectively.

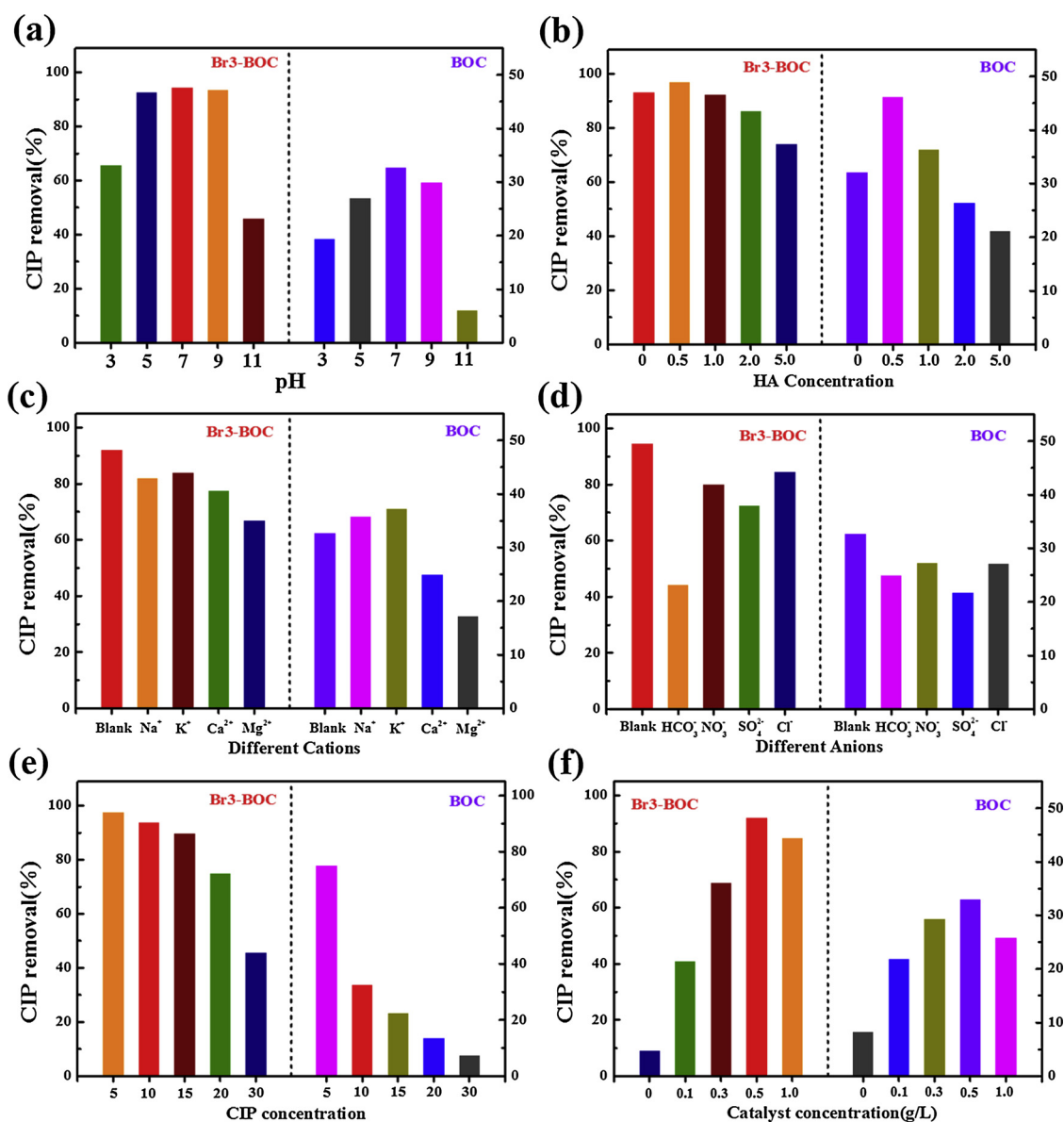
Based on these results, it is believed that the pathway of CIP degradation might be different in the presence of BOC and Br-doped BOC samples. It is reported that the antibacterial activity of CIP solution is highly related to the group structural of CIP, and different structural groups possess different bacteriostasis [34,35]. Therefore, the difference in TOC removal and antibacterial activity of CIP solution over BOC and Br3-BOC should be attributed to the different intermediates in CIP degradation. In order to clarify the photodegradation pathway of CIP over BOC and Br3-BOC, HPLC-MS spectra are performed to analyze the intermediates of CIP degradation in the presence of BOC and Br3-BOC,

respectively. The MS spectra of the intermediates of CIP degradation over BOC and Br3-BOC are listed in Figs. S5 and S6 (Supporting Information), and the proposed structural formulas of the major fragment ions in mass spectra are listed in Table S3 (Supporting Information). Combined with the data analysis and literatures [36–38], the main intermediate products and degradation pathway of CIP over BOC (pathway I) and Br3-BOC (pathway I and pathway II) are proposed, as illustrated in Scheme 1. In the presence of BOC, the main pathway of CIP degradation is the destruction of piperazine ring (pathway I). Noticeably, both the piperazine ring opening process (pathway I) and pyrrole ketone ring opening process (pathway II) occurs in the CIP degradation over Br3-BOC. It is proposed that the destruction of pyrrole ketone ring caused by strong oxidation ability of  $\cdot O_2^-$  leads to the loss of antibacterial ability of the CIP degradation solution in the presence of Br3-BOC. The generated  $\cdot OH$  and  $h^+$  in BOC could only destroy the piperazine ring of CIP, which still remains a strong inhibitory effect on *E. coli* [34].

For practical application in antibiotics water treatment, the effects of various factors including pH values, organic matters, cations, anions, CIP concentrations and catalyst dosages on the degradation efficiency of CIP should be considered. As shown in Fig. 9, the Br3-BOC sample shows higher photocatalytic efficiency for CIP degradation in a relative wide pH range (pH = 5–9), while the photocatalytic efficiency of CIP degradation over BOC decreases under acidic and basic conditions (Fig. 9a). As the typical organic matter in the environmental wastewater, humic acid (HA) is chosen to investigate the effect of organic matters on the CIP degradation. It is found that low concentration HA has slight influence on the CIP degradation over Br3-BOC, however, high concentration HA could inhibit the CIP degradation over Br3-BOC. In the presence of BOC, low concentration HA contributes to CIP degradation, and high concentration inhibits the CIP degradation (Fig. 9b). Fig. 9c shows the CIP degradation efficiency over BOC and Br3-BOC in the presence of different cationic ions, including  $Na^+$ ,  $K^+$ ,  $Ca^{2+}$  and  $Mg^{2+}$  ions, respectively. It reveals that  $Ca^{2+}$  and  $Mg^{2+}$  could obviously inhibit the CIP degradation, and  $Na^+$  and  $K^+$  shows little inhibitory effect on the CIP degradation, both in BOC and Br3-BOC system. Besides,  $HCO_3^-$ ,  $NO_3^-$ ,  $SO_4^{2-}$  and  $Cl^-$  are selected to explore



Scheme 1. Proposed photocatalytic degradation pathways of CIP.

Fig. 9. The effects of pH values (a), organic matter (b), cations (c), anions (d), CIP concentrations (e) and catalyst dosage (f) on the degradation of CIP over Br<sub>3</sub>-BOC.

the effect of anion on the CIP degradation. As shown in Fig. 9d, it is found that all the anion could inhibit the CIP degradation both in BOC and Br3-BOC system. Among them,  $\text{HCO}_3^-$  ions show more obvious inhibitory effect on the CIP degradation. Moreover, the effects of the CIP concentration and the catalyst dosage on the photodegradation efficiency are also discussed (Fig. 9e and f). With the increase of the CIP concentration, the photodegradation efficiency decreases readily, especially in the BOC system. It is also found that the increase of catalyst dosage could promote the CIP removal rate, and slight decrease in CIP removal rate is observed when the amount of photocatalyst (BOC or Br3-BOC) increases to a certain value (0.5 g/L), which might be meaningful for the input of photocatalyst in the practical CIP degradation. Moreover, the stability of the photocatalyst was also determined. The recycle experiments of BOC and Br3-BOC for the CIP photodegradation (Fig. S7, Supporting Information) demonstrated that both BOC and Br3-BOC still remained its original photocatalytic ability after five cycles of photodegradation, implying the good stability for CIP degradation.

#### 4. Conclusions

In this work, we propose a strategy for the activation of molecular oxygen through a simple method of bromine doping. With the doping of bromine, the energy level of  $\text{Bi}_2\text{O}_2\text{CO}_3$  are mediated, which provides a more negative conduction band position for the molecular oxygen activation. Moreover, bromine doping promotes the charge separation and restricts the recombination of electrons and holes, also resulting in the enhancement of molecular oxygen activation. As expected, Br-doped BOC shows higher efficiency of CIP degradation and mineralization rate than that of BOC, which is attributed to the generation of  $\cdot\text{O}_2^-$ . More importantly, Br-doped BOC sample undergoes two pathways during the CIP degradation, which involves in the piperazine ring opening process and pyrrole ketone ring opening process. It results in the loss of the antibacterial ability towards *E. coli* the degradation products, which could avoid drug resistance and the second pollution effectively. This study not only provides a convenient strategy for the activation of molecular oxygen, but also realizes the meaningful degradation of CIP in practical water treatment.

#### Declaration of Competing Interest

None.

#### Acknowledgements

This work was supported by the National Natural Science Foundation of China (21671153 and 21601141), Department of Education of Hubei Province under the project of Science and Technology Innovation Team of Outstanding Young and Middle-aged Scientists (T201606), and Hubei Superior and Distinctive Discipline Group of "Mechatronics and Automobiles" (XKQ2019058). The author would like to thank Zou Yun from Shiyanjia Lab ([www.shiyanjia.com](http://www.shiyanjia.com)) for the DFT calculation.

#### Appendix A. Supplementary data

Supplementary material related to this article can be found, in the online version, at doi:<https://doi.org/10.1016/j.apcatb.2019.117966>.

#### References

- [1] S. Zhao, Z. Dai, W. Guo, F. Chen, Y. Liu, R. Chen, Highly selective oxidation of glycerol over  $\text{Bi}/\text{Bi}_{3.64}\text{Mo}_{0.36}\text{O}_{6.55}$  heterostructure: dual reaction pathways induced by photogenerated  $\cdot\text{O}_2^-$  and holes, *Appl. Catal. B: Environ.* 244 (2019) 206–214.
- [2] L. Wang, K. Xu, W. Cui, D. Lv, L. Wang, L. Ren, X. Xu, F. Dong, S.X. Dou, W. Hao, Y. Du, Monolayer epitaxial heterostructures for selective visible light driven photocatalytic NO oxidation, *Adv. Funct. Mater.* 29 (2019) 1808084.
- [3] N. Chen, H. Shang, S. Tao, X. Wang, G. Zhan, H. Li, Z. Ai, J. Yang, L. Zhang, Visible light driven organic pollutants degradation with hydrothermally carbonized sewage sludge and oxalate via molecular oxygen activation, *Environ. Sci. Technol.* 52 (2018) 12656–12666.
- [4] X. Ding, K. Zhao, L. Zhang, Enhanced photocatalytic removal of sodium pentachlorophenate with self-doped  $\text{Bi}_2\text{WO}_6$  under visible light by generating more superoxide ions, *Environ. Sci. Technol.* 48 (2014) 5823–5831.
- [5] H. Wang, S. Chen, D. Yong, X. Zhang, S. Li, W. Shao, X. Sun, B. Pan, Y. Xie, Giant electron-hole interactions in confined layered structures for molecular oxygen activation, *J. Am. Chem. Soc.* 139 (2017) 4737–4742.
- [6] J. Ding, Z. Dai, F. Qin, H. Zhao, S. Zhao, R. Chen, Z-scheme  $\text{BiO}_{1-x}\text{Br}/\text{Bi}_2\text{O}_2\text{CO}_3$  photocatalyst with rich oxygen vacancy as electron mediator for highly efficient degradation of antibiotics, *Appl. Catal. B: Environ.* 205 (2017) 281–291.
- [7] K. Zhao, L. Zhang, J. Wang, Q. Li, W. He, J.J. Yin, Surface structure-dependent molecular oxygen activation of  $\text{BiOCl}$  single-crystalline nanosheets, *J. Am. Chem. Soc.* 135 (2013) 15750–15753.
- [8] Y. Zheng, Z. Yu, H. Ou, A. Asiri, Y. Chen, X. Wang, Black phosphorus and polymeric carbon nitride heterostructure for photoinduced molecular oxygen activation, *Adv. Funct. Mater.* 27 (2018) 1705407.
- [9] N. Siemer, A. Luken, M. Zalibera, J. Frenzel, D. Munoz-Santiburio, A. Savitsky, W. Lubitz, M. Muhler, D. Marx, J. Strunk, Atomic scale explanation of  $\text{O}_2$  activation at the Au- $\text{TiO}_2$  interface, *J. Am. Chem. Soc.* 140 (2018) 18082–18092.
- [10] S. Han, C. Mullins, Surface alloy composition controlled  $\text{O}_2$  activation on Pd–Au bimetallic model catalysts, *ACS Catal.* 8 (2018) 3641–3649.
- [11] J. Ding, Z. Dai, F. Tian, B. Zhou, B. Zhao, H. Zhao, Z. Chen, Y. Liu, R. Chen, Generation of defect clusters for  $\cdot\text{O}_2^-$  production for molecular oxygen activation in photocatalysis, *J. Mater. Chem. A* 5 (2017) 23453–23459.
- [12] H. Huang, S. Tu, C. Zeng, T. Zhang, A.H. Reshak, Y. Zhang, Macroscopic polarization enhancement promoting photo- and piezoelectric-induced charge separation and molecular oxygen activation, *Angew. Chemie Int. Ed.* 56 (2017) 11860–11864.
- [13] Z. Dai, F. Qin, H. Zhao, J. Ding, Y. Liu, R. Chen, Crystal defect engineering of Aurivillius  $\text{Bi}_2\text{MoO}_6$  by Ce doping for increased reactive species production in photocatalysis, *ACS Catal.* 6 (2016) 3180–3192.
- [14] M. Shim, P. Guyot-Sionnest, n-type colloidal semiconductor nanocrystals, *Nature* 407 (2000) 981–983.
- [15] S.H. Zhang, Heather M. Moudgil, Kartikay Richter, Curt A. Hight Walker, Angela R. Barlow, Stephen Marder, Seth R. Hacker, Christina A. Pookpanratana, J. Sujitra, Controllable, wide-ranging n-doping and p-doping of monolayer group 6 transition-metal disulfides and diselenides, *Adv. Mater.* 30 (2018) 1802991.
- [16] F.J. Himpsel, G. Hollinger, R.A. Pollak, Determination of the fermi-level pinning position at  $\text{Si}(111)$  surfaces, *Phys. Rev. B* 28 (1983) 7014–7018.
- [17] Y. Shi, Y. Zhou, D.R. Yang, W.X. Xu, C. Wang, F.B. Wang, J.J. Xu, X.H. Xia, H.Y. Chen, Energy level engineering of  $\text{MoS}_2$  by transition-metal doping for accelerating hydrogen evolution reaction, *J. Am. Chem. Soc.* 139 (2017) 15479–15485.
- [18] F. Tian, H. Zhao, Z. Dai, G. Cheng, R. Chen, Mediation of valence band maximum of  $\text{BiOI}$  by Cl incorporation for improved oxidation power in photocatalysis, *Ind. Eng. Chem. Res.* 55 (2016) 4969–4978.
- [19] H. Huang, X. Li, J. Wang, F. Dong, P.K. Chu, T. Zhang, Y. Zhang, Anionic group self-doping as a promising strategy: band-gap engineering and multi-functional applications of high-performance  $\text{CO}_3^{2-}$ -doped  $\text{Bi}_2\text{O}_2\text{CO}_3$ , *ACS Catal.* 5 (2015) 4094–4103.
- [20] H. Zhao, G. Li, F. Tian, Q. Jia, Y. Liu, R. Chen, g- $\text{C}_3\text{N}_4$  surface-decorated  $\text{Bi}_2\text{O}_2\text{CO}_3$  for improved photocatalytic performance: theoretical calculation and photodegradation of antibiotics in actual water matrix, *Chem. Eng. J.* 366 (2019) 468–479.
- [21] Y. Zhou, H. Wang, M. Sheng, Q. Zhang, Z. Zhao, Y. Lin, H. Liu, G.R. Patzke, Environmentally friendly room temperature synthesis and humidity sensing applications of nanostructured  $\text{Bi}_2\text{O}_2\text{CO}_3$ , *Sens. Actuators B: Chem.* 188 (2013) 1312–1318.
- [22] H. Gan, G. Zhang, H. Huang, Enhanced visible-light-driven photocatalytic inactivation of *Escherichia coli* by  $\text{Bi}_2\text{O}_2\text{CO}_3/\text{Bi}_3\text{NbO}_7$  composites, *J. Hazard. Mater.* 250 (2013) 131–137.
- [23] S. Peng, L. Li, H. Tan, Y. Wu, R. Cai, H. Yu, X. Huang, P. Zhu, S. Ramakrishna, M. Srinivasan, Q. Yan, Monodispersed Ag nanoparticles loaded on the PVP-assisted synthetic  $\text{Bi}_2\text{O}_2\text{CO}_3$  microspheres with enhanced photocatalytic and supercapacitive performances, *J. Mater. Chem. A* 1 (2013) 7630–7638.
- [24] S. Lin, W. Cui, X. Li, H. Sui, Z. Zhang,  $\text{Cu}_2\text{O}$  NPs/ $\text{Bi}_2\text{O}_2\text{CO}_3$  flower-like complex photocatalysts with enhanced visible light photocatalytic degradation of organic pollutants, *Catal. Today* 297 (2017) 237–245.
- [25] X. Xiong, T. Zhou, X. Liu, S. Ding, J. Hu, Surfactants-mediated synthesis of single-crystalline  $\text{Bi}_3\text{O}_4\text{Br}$  nanorings with enhanced photocatalytic activity, *J. Mater. Chem. A* 5 (2017) 15706–15713.
- [26] Z. Ni, Y. Sun, Y. Zhang, F. Dong, Fabrication, modification and application of  $(\text{BiO})_2\text{CO}_3$ -based photocatalysts: a review, *Appl. Surf. Sci.* 365 (2016) 314–335.
- [27] T. Xiong, Xa. Dong, H. Huang, W. Cen, Y. Zhang, F. Dong, Single precursor mediated-synthesis of Bi semimetal deposited N-doped  $(\text{BiO})_2\text{CO}_3$  superstructures for highly promoted photocatalysis, *ACS Sustain. Chem. Eng.* 4 (2016) 2969–2979.
- [28] Y. Zhou, Z. Zhao, F. Wang, K. Cao, D.E. Doronkin, F. Dong, J.D. Grunwaldt, Facile synthesis of surface N-doped  $\text{Bi}_2\text{O}_2\text{CO}_3$ : origin of visible light photocatalytic activity and in situ DRIFTS studies, *J. Hazard. Mater.* 307 (2016) 163–172.
- [29] H. Zhao, J. Tang, Q. Lai, G. Cheng, Y. Liu, R. Chen, Enhanced visible light photocatalytic performance of Sb-doped  $(\text{BiO})_2\text{CO}_3$  nanoplates, *Catal. Commun.* 58 (2015) 190–194.
- [30] J. Zai, F. Cao, N. Liang, K. Yu, Y. Tian, H. Sun, X. Qian, Rose-like I-doped  $\text{Bi}_2\text{O}_2\text{CO}_3$  microspheres with enhanced visible light response: DFT calculation, synthesis and

- photocatalytic performance, *J. Hazard. Mater.* 321 (2017) 464–472.
- [31] S. Wang, X. Ding, X. Zhang, H. Pang, X. Hai, G. Zhan, W. Zhou, H. Song, L. Zhang, H. Chen, J. Ye, In situ carbon homogeneous doping on ultrathin bismuth molybdate: a dual-purpose strategy for efficient molecular oxygen activation, *Adv. Funct. Mater.* 27 (2017) 1703923.
- [32] Y. Liu, Y. Lv, Y. Zhu, D. Liu, R. Zong, Y. Zhu, Fluorine mediated photocatalytic activity of BiPO<sub>4</sub>, *Appl. Catal. B: Environ.* 147 (2014) 851–857.
- [33] X. Xu, X. Ding, X. Yang, P. Wang, S. Li, Z. Lu, H. Chen, Oxygen vacancy boosted photocatalytic decomposition of ciprofloxacin over Bi<sub>2</sub>MoO<sub>6</sub>: oxygen vacancy engineering, biotoxicity evaluation and mechanism study, *J. Hazard. Mater.* 364 (2019) 691–699.
- [34] H.S. Ou, J.S. Ye, S. Ma, C.H. Wei, Y.G. N, J.Z. He, Degradation of ciprofloxacin by UV and UV/H<sub>2</sub>O<sub>2</sub> via multiple-wavelength ultraviolet light-emitting diodes: effectiveness, intermediates and antibacterial activity, *Chem. Eng. J.* 289 (2016) 391–401.
- [35] X. Zhang, R. Li, M. Jia, S. Wang, Y. Huang, C. Chen, Degradation of ciprofloxacin in aqueous bismuth oxybromide (BiOBr) suspensions under visible light irradiation: a direct hole oxidation pathway, *Chem. Eng. J.* 274 (2015) 290–297.
- [36] X.J. Wen, C.G. Niu, L. Zhang, C. Liang, H. Guo, G.M. Zeng, Photocatalytic degradation of ciprofloxacin by a novel Z-scheme CeO<sub>2</sub>-Ag/AgBr photocatalyst: influencing factors, possible degradation pathways, and mechanism insight, *J. Catal.* 358 (2018) 141–154.
- [37] H. Tang, Z. Dai, X. Xie, Z. Wen, R. Chen, Promotion of peroxydisulfate activation over Cu<sub>0.84</sub>Bi<sub>2.08</sub>O<sub>4</sub> for visible light induced photodegradation of ciprofloxacin in water matrix, *Chem. Eng. J.* 356 (2019) 472–482.
- [38] K. Wang, Y. Li, G. Zhang, J. Li, X. Wu, 0D Bi nanodots/2D Bi<sub>2</sub>NbO<sub>7</sub> nanosheets heterojunctions for efficient visible light photocatalytic degradation of antibiotics: enhanced molecular oxygen activation and mechanism insight, *Appl. Catal. B: Environ.* 240 (2019) 39–49.